Characterization of expanded austenite developed on AISI 316L stainless steel by plasma carburization

J. García Molleja [a], L. Nosei [b], J. Ferrón [c], E. Bemporad [d], J. Lesage [e], D. Chicot [e], J. Feugeas [a,*]

[a] *Instituto de Física Rosario (CONICET-UNR), Bvrd. 27 de Febrero 210 Bis., 2000 Rosario, Argentina*
[b] *Instituto de Mecánica Aplicada y Estructuras (FCEIA-UNR), Berutti y Riobamba, 2000 Rosario, Argentina*
[c] *Instituto de Desarrollo Tecnológico para la Industria Química (CONICET-UNL), Güemes 3450, 3000 Santa Fe, Argentina*
[d] *University Roma Tre, Mechanical and Industrial Engineering Department, Via della Vasca Navale 79, 00146 Rome, Italy*
[e] *Laboratoire de Mécanique de Lille UMR 8107, University of Science and Technology of Lille, BP 179, 59653 Villeneuve d'Ascq Cedex, France*

ARTICLE INFO

ABSTRACT

Expanded austenite generation through ion carburizing of AISI 316L using two different reactive gas mixtures (Ar 50%, H_2 45%, CH_4 5% and Ar 80%, H_2 15%, CH_4 5%) has been studied. It was found that an ~14 µm surface layer of expanded austenite was developed with 30 min processing for both gas mixtures. Nevertheless, AES analyses have shown that on the ~150 nm surface layer carbon in a concentration of ~12% was diffused and located as carbide. For longer periods of processing, while for the gas mixture with 50% of Ar no significant modifications within those 150 nm surface layer were produced, for the gas mixture with 80% of Ar a gradual increase in the carbon concentration with time was found, with the extra carbon remaining as free carbon. The difference between both situations can be attributed to the different resulting current densities that have been of 7.0 mA cm^{-2} and 8.1 mA cm^{-2} for 50% and 80% of Ar respectively. Higher current densities result in higher carbon and Ar ions fluxes inducing, from one side surface element concentration modification through sputtering, and from the other the enhancement of carbon diffusion on the first hundred nanometers of the surface layers. This free carbon on top of the surface layers can act as solid lubricant reducing wear rate. Nevertheless, and in spite of the fact that expanded austenite was proved to be corrosion resistant, a reduction against NaCl solution corrosion in relation to the base material was observed. This lost to corrosion resistance can be attributed to carbide development on the layers closer to the surface that can work as a trigger for localized corrosion.

© 2010 Elsevier B.V. All rights reserved.

1. Introduction

Expanded austenite (EA) development on austenitic stainless steel (ASS) has been studied for many years principally motivated by the possibility of giving the surface higher wear resistance and hardening without introducing substantial worsening in their corrosion behavior. Customary, the development of EA has been practiced through low-temperature nitriding, carburization or nitro-carburization using different techniques, most of which are based on plasmas generation. A case in point are the ones based on glow discharges [1–4], plasma immersion ion implantation (PIII) [5–8], low energy ion implantation [9,10], among others. In all cases nitrogen (pure or a mixture with others like hydrogen) was used for nitriding processes, meanwhile low molecular weight hydrocarbons (principally methane) mixed with other gases like hydrogen, argon, etc., were used in carburization processes. Also, experiments of nitro-carburization had been developed obtaining layers in which both nitrogen and carbon species were

introduced into the ASS surface with development of EA [11]. In spite of the surface hardening and the wear rate reduction, the EA behavior under corrosion, compared with the one of the original ASS, is not totally resolved and the results reported differ among several authors. While some of them consider that the corrosion resistance increases, others have found apparently no modifications and others indeed have concluded that there was some worsening [5,12]. F. Ernst et al. [13] have found, using low-temperature (<475 °C) gas-phase carbiding, that the corrosion behavior is correlated to the possibility of carbide formation. Indeed, for a pure EA layer an effective corrosion resistance improvement has been found, while with carbides the effect is the opposite, i.e. the development of corrosion becomes important.

The lattice parameters for EA developed under dual nitro-carburization processes using PIII technology [14] have been studied, showing the coexistence of two fcc structures corresponding to nitrogen and carbon solid solutions, with a maximum lattice expansion of 7.5% and 2.1% for each of them respectively, values that coincide with the ones of other authors [15]. Also, this double-layer structure was observed in plasma assisted nitriding before the proper low-temperature (T < 42 °C) nitriding in a N_2–H_2 gas mixture, a

* Corresponding author. Tel.: +54 341 4853222; fax: +54 341 4821772.
 E-mail address: feugeas@ifir-conicet.gov.ar (J. Feugeas).

pre-cleaning with an Ar–H_2 was performed to remove oxides of the surface [16]. Nevertheless, carbon contaminates the surface during sample pre-heating. Then, when the pre-cleaning process of the surface is activated, the O_2 is removed but not carbon that will diffuse down in the sample helped by the temperature, developing a γ_C layer. When the nitriding process starts, a γ_N is developed pushing the γ_C down becoming an inter-phase between the γ_N and the bulk. Nevertheless, this inter-phase γ_C layer was not observed when the ion nitriding was not preceded by the in-situ pre-cleaning process. T. Christiansen et al. [17] have studied free stress EA generated through gaseous nitriding finding that it corresponds to a pure fcc crystal lattice structure. Their studies have shown that EA lattice parameter measurement variation found in the literature can be attributed to other secondary effects like strong stresses induced during the nitriding, carburization or nitro-carburization processes, with the consequent development of defects inside the grains like stacking faults, sliding bands, twins, etc., which generate asymmetric strains according to different crystallographic planes [11].

D.L. Williamson et al. [9] attribute nitrogen diffusion behavior to nitrogen trapped in the chromium sites inside lattice, which induces a much higher nitrogen super-saturation together with a reduction in its diffusivity in comparison with carbon diffusion. Carbon, which has a weaker interaction with chromium, diffused faster into the ASS but at a lower saturation rate. Nevertheless, they conclude that in spite of the difference between nitrogen and carbon, both remain in solid solution, presumably on interstitial sites. In particular for carburized AISI 316L ASS, Auger Electron Spectroscopy (AES) and Electron Dispersion Spectroscopy (EDS) analyses, carbon levels higher than 12 at.%, without any evidence of carbide precipitation have been shown. On the other hand, other authors [13,18] have proposed that in a gas-phase carburizing below 470 °C and during periods $\leq$36 h, substitutional elements like carbon can rapidly diffuse in the AISI 316L ASS reaching a colossal carbon super-saturation with carbon concentration percentages of ~12% (γ_C) but without carbide precipitation. At this point the degree of expansion of austenite reduces the initial metal atom volume misfit between γ_C and χ to a level that substantially reduces the contribution of misfit strain energy to the nucleation barrier. Then, if the carburizing process continues for longer periods, χ or Hägg carbides (Fe_5C_2) begin to precipitate. Also, they proposed that nucleation and growth of carbides could be related to the relative crystal lattices orientation between γ_C and χ at the interface.

In this paper we have studied wear, hardness and corrosion property modifications of AISI 316L ASS after ion carbiding at low temperature and low processing times.

2. Experimental

2.1. Ion carburization process

Samples of AISI 316L ASS were cut, machined and polished with sizes and geometries according to testing purposes. Polishing process consisted in grinding with abrasive papers of different granulometry (80 to 1200), ending with a suspension of 1 μm alumina powder in water. The final rugosity was measured using a Surface Roughness Tester, Model TR 200, using a diamond point with an angle of 90 with a load of 4 mN, giving a final resolution of 10–40 nm. The results have shown a Ra (mean values between top of the peaks and valleys) of ~40 nm and ~130 nm before and after carburizing. Before being introduced in the carburization chamber, samples were degreased and cleaned beginning with ethanol and ending with acetone.

Carburization was performed in the 8 L capacity glow discharge reactor (Rosario Institute of Physics) already described for ion nitriding processes in Ref. [19]. Two different gas processing mixtures: a — Ar 50%, H_2 45%, CH_4 5%, and b — Ar 80%, H_2 15%, CH_4 5%; with three different processing times: 30, 60 and 120 min have been used. In all cases the gas mixture pressure was 5.00 ± 0.01 mbar and the processing temperature 405 ± 5 °C. The temperature was controlled by the applied voltage on the cathode (sample holder) that it was of 550 ± 15 V for the gas mixture a, and of 460 ± 45 V for gas mixture b. The resulting current density on samples was 7.0 ± 0.4 mA cm^{-2} and 8.10 ± 0.5 mA cm^{-2} for gas mixtures a and b respectively. Once carburized, samples were left to cool down to room temperature inside the chamber in an atmosphere of argon at low pressure, before being removed for characterization tests. In Table 1 samples used in this work are identified according to the processing parameters.

2.2. Sample characterization

2.2.1. X-ray diffraction

X-ray diffraction measurements were done in the glancing mode (GAXRD) with a Philips X'Pert using the Cu-Kα line corresponding to a wavelength of 1.54 Å. The angle of incidence used was 10°. Considering the X-ray energy corresponding to the Cu-Kα emission line (~8 keV), the mass attenuation coefficient for Fe ($\mu = 2480$ cm^{-1}), and an intensity attenuation appreciation limit of 1%, the estimated thickness of the X-ray observed layer for the 10° incidence angle used has been approximately 3 μm. The use of the mass attenuation for Fe is justified because the AISI 316L ASS has ~70% of Fe and ~17% Cr in their composition, with only ~10% of Ni.

All diffractograms of carburized samples have shown the same structure, with the peaks corresponding to planes (111), (200) and (202), which can be associated to an fcc structure with the 2θ reflected angles corresponding to a typical EA structure [4,5,11,19]. As an example, in Fig. 1 the diffractogram corresponding to sample B1 is displayed (dashed trace) showing the peaks corresponding to planes (111), (200) and (202) at 42.830°, 49.530° and 73.170° respectively. For comparative purposes, in the same figure the diffractogram corresponding to the base material (continuous trace) is also displayed with the peaks of planes (111), (200) and (202) at 43.625°, 50.675° and 74.765° respectively, showing the typical structure of austenite. Nevertheless, there was observed a systematic decrease of reflected 2θ angles (corresponding to the three peaks) with increasing processing times for both gas mixtures used. This behavior can be seen on Fig. 2, where the lattice parameters are plotted as a function of processing time, and for both gas mixtures. The lattice parameters used in this figure were evaluated using the Nelson–Riley extrapolation function (the lattice parameters versus $\cot g(\theta) \cdot \cos(\theta)$) [16].

2.2.2. Auger Electron Spectroscopy

Element concentration profiles were studied using Auger Electron Spectroscopy (AES). An Auger spectrum was first taken in the surface, and then at different depths, by sequentially removing layers of material using sputtering with Ar ions. This procedure has allowed plotting the concentration of each element at different depths down to the maximum explored depth i.e. ~156 nm (corresponding to 65 min sputtering) or at the depth at which the concentrations become almost constant. Deeper measurements were not convenient because of the lack of accuracy of the estimation depths. The results are displayed in Figs. 3–5. In Figs. 3 and 4 it is possible to see the AES

Table 1

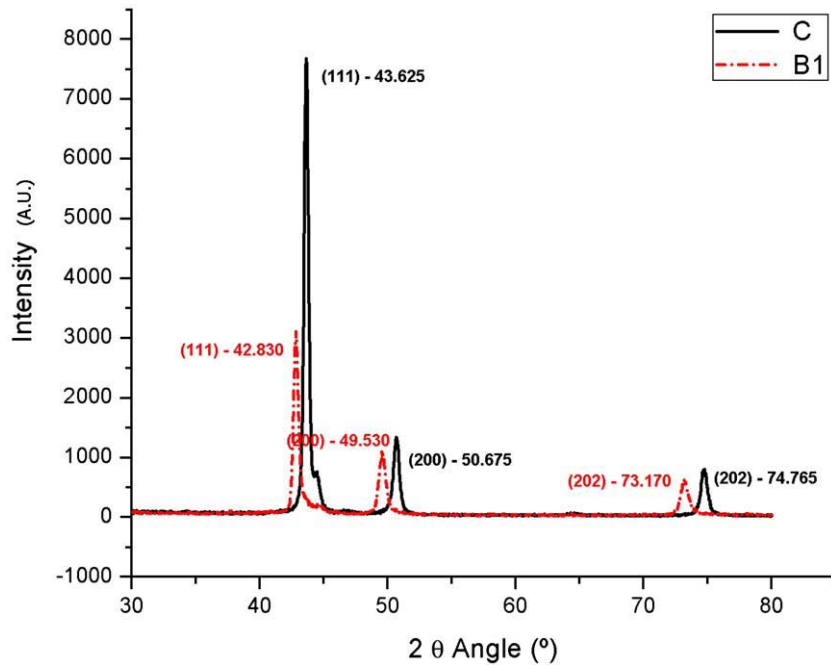| Sample	Gas mixture	Processing time
A1	Ar 50%, H_2 45%, CH_4 5%	30 min
A2	''	60 min
A3	''	120 min
B1	Ar 80%, H_2 15%, CH_4 5%	30 min
B2	''	60 min
B3	''	120 min
C	Non-Carburized	–

Fig. 1. GAXRD diffractograms (corresponding to an incidence angle of 10°) showing comparatively the planes (111), (200) and (202) 2θ reflected angle peaks corresponding to EA generated on carburized sample B1 and to the austenite of the non-carburized AISI 316L ASS.

spectra results for samples A1 and A3, and B1, B2 and B3 respectively showing concentration profiles of more abundant alloying elements of the steel (i.e. Fe, Cr and Ni), carbon and O_2. Looking at the results corresponding to samples A1 and A3 (parts a and b of Fig. 3) we can see that the Fe concentration becomes almost constant ($\sim$62% and $\sim$63% for A1 and A3 respectively) below 10 min sputtering ($\sim$25 nm), concentrations that are rapidly reduced toward the surface. Chromium instead, has a little variation from the surface to the lower layer inspected (corresponding to 65 min sputtering), at which a concentration of $\sim$18% is reached. Also, carbon shows almost constant concentration profiles ($\sim$15% and $\sim$14% for A1 and A3 respectively) except for the first nanometers in which higher values can be seen but that can be attributed to the surface contamination during the AES analyses.

On the other hand, the results on samples processed with the other gas mixture (B1, B2 and B3) are substantially different. In this case there is a clear influence of the carburization time on the concentration profiles. On sample B1 (part a of Fig. 4), Fe concentration, which is $\sim$35%

on the surface (owing the value measured on top of the surface), grows fast up to $\sim$52% after 5 min sputtering ($\sim$15 nm) continuing with a lower growing rate reaching 60% after 60 min of sputtering ($\sim$145 nm). Carbon, that has a concentration of $\sim$30% on the surface, is reduced to $\sim$25% after 5 min sputtering ($\sim$15 nm), followed by a slow decreasing

Fig. 3. Auger atomic concentration profiles corresponding to samples A1 and A3.
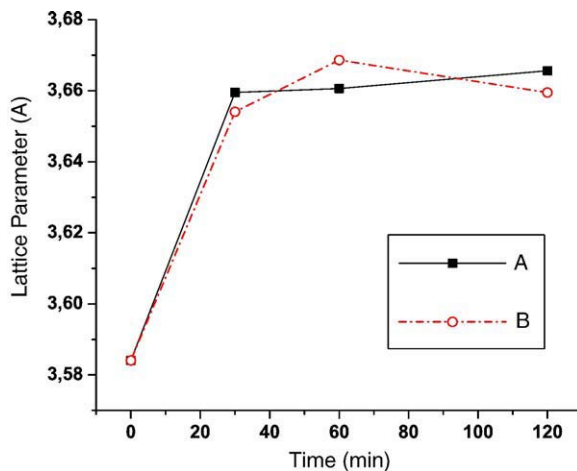

Fig. 2. EA lattice parameter versus carburization time for samples treated with the gas mixture Ar 50%, H_2 45%, CH_4 5% (A) and Ar 80%, H_2 15%, CH_4 5% (B).
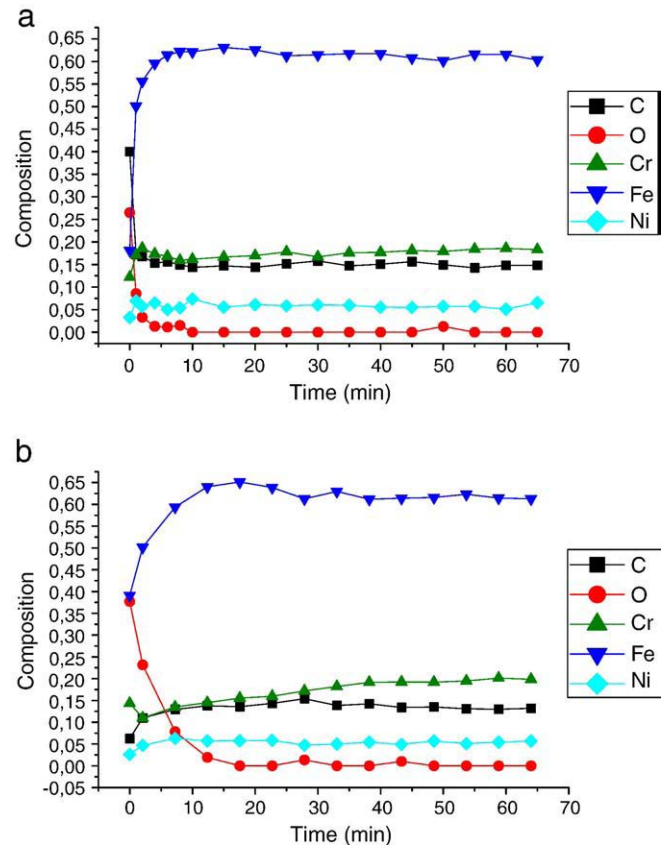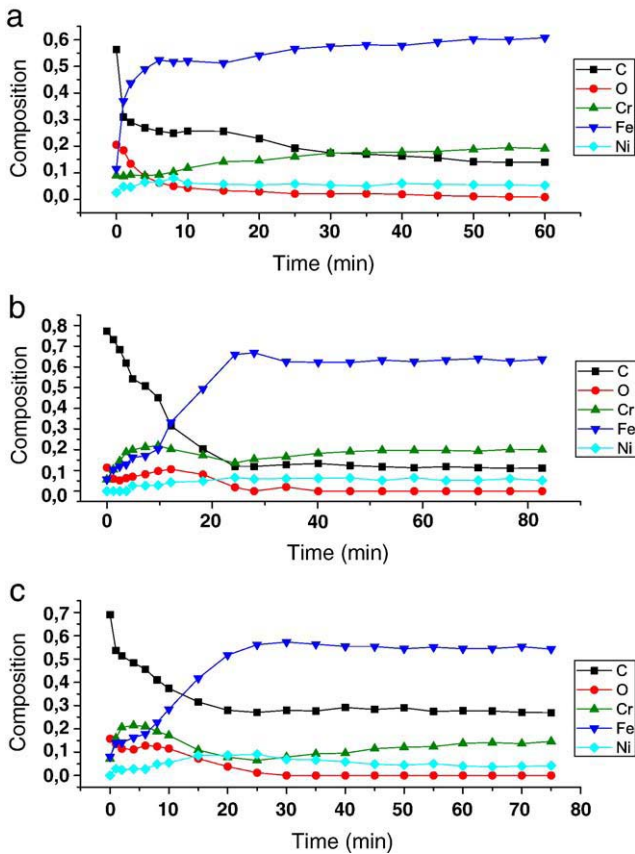
Fig. 4. Auger atomic concentration profiles corresponding to samples B1, B2 and B3.

down to the lower explored depth were the concentration results ~15%. Chromium instead, has a concentration of ~9% at the surface growing at a low rate up to ~19% at the maximum explored depth.

Same analysis for sample B2 (part b of Fig. 4) shows that Fe concentration, which is ~10% on the surface (also in this case we have ignored the values on top of the surface), grows with a high rate reaching ~66% after 22 min sputtering (~50 nm), continuing with a constant value of ~63% down to the maximum depth. Carbon instead, which has a concentration of ~72% at the surface, decreases down to ~14% after the 22 min sputtering, decreasing continuously down to ~11% at the maximum depth. Nevertheless chromium has a different behavior. Meanwhile its concentration grows at slow rate below the first ~50 nm (corresponding to 22 min sputtering), the closer to the surface concentration profile has a dome shape with a maximum of ~22% after 7 min sputtering.

Sample B3 has a similar qualitative behavior (part c of Fig. 4) than B2. Fe has a surface concentration of ~14% growing up to ~58% after 22 min sputtering followed by a slow decrease down to ~55% at the maximum explored depth. Finally carbon, which has a concentration of ~54% at the surface gradually decreases to ~28% at after 22 min sputtering remaining constant down to the maximum explored depth. Chromium, which has a concentration of ~6% after 22 min sputtering, grows up to ~16% at the maximum explored depth. Nevertheless, like for sample B2, the closer to the surface concentration profile presents a dome shape with a maximum concentration of ~21% after 5 min sputtering.

In Fig. 5, total carbon concentration versus sputtering time is plotted for samples A1, A3, B1, B2 and B3 (parts a, b, c, d and e respectively). The results of samples A1 and A3 show an almost constant (~14%) carbon concentration with depth from the first 2 min of sputtering to the maximum explored depth. Nevertheless, results of samples B1, B2 and B3 are different. Carbon concentration, which

becomes constant after the first ~25 min sputtering (~13%, ~12% and ~29% for B1, B2 and B3 respectively), grows up reaching their maximum on the surface (~30%, ~73% and ~60% for B1, B2 and B3 respectively, owing the values on top of the surface). However, a close inspection of the shape evolution of the Auger lines clearly shows that AES contains also information about the chemical state of the elements along these profiles. In Fig. 6 we depict a couple of snapshots along the depth profile showing the shape of carbon Auger line. The points correspond (as example) to sample B1 at the beginning, at some intermediate and final point of the profile. The high energy part of the spectra shows the disappearance of the oxygen peak and the appearance of the Cr and Fe ones, ending with a pure Fe–Cr–C alloy. However, the point we want to emphasize here is the change of shape observed in the carbon line, where the first corresponds to an almost pure "graphite" (non-chemically bounded carbon) shape meanwhile the last corresponds to "carbide" (chemically bounded carbon) one [20].

Although, X-ray Photoelectron Spectroscopy (XPS) is the most relevant technique for the surface chemical analysis, when spatial resolution like in depth profiling is needed, Auger may be successfully applied. Auger line shape contains the chemical information that can be obtained through Factor Analysis (FA) calculations [21]. The FA method is currently included as a standard package in most data treatment, and we have successfully applied it to several problems using AES [22–24].

Indeed, in parts a, b, c, d and e of Fig. 5 together with the total concentration profiles, the percentage of free and chemically bounded carbon were also plotted versus sputtering time, showing that after several tens of minutes of sputtering time, most of the carbon has turned out to be chemically bounded. Nevertheless, the closer to the surface layers, a chemically bounded against free carbon ratio variation with sputtering time can be appreciated. Meanwhile at the top of the surface of all samples 100% of carbon was found as free carbon, the depth profiles were different among themselves. In cases of samples A1 and A3, the carbon after the first 2 min of sputtering time was totally chemically bounded. On the other hand, for sample B1, a rapid free carbon concentration reduction to negligible values after 15 min sputtering could be appreciated, meanwhile for sample B2, free carbon concentration had a much slower reduction becoming negligible at depths corresponding to 25 min sputtering. For sample B3 instead, a gradual free carbon concentration reduction could be observed, becoming negligible later after 60 min sputtering.

2.2.3. Expanded austenite layer observation

The layers of EA have been studied under optical microscopy and Focused Ion Beams (FIB). Using optical microscopy, the samples' surfaces have been studied as removed from the treatment's chamber, as well as the samples' cross section by cross cutting, polishing and electrochemically etching them in a 10% solution of oxalic acid in water. In Fig. 7 the surface (part a) and the cross section (part b) of a sample A1 can be seen. The surface of the steel after being treated shows the typical structure of austenite after a cold working process (sliding bands), but without visible grains deformations. The cross section shows an ~14 μm surface layer with a structure corresponding to the EA, with a typical structure of austenite in the bulk, below the first 14 μm. The continuity of the grain boundaries through the interface is not observed due to the good resistance of the EA to the electrochemical etching specifically used to show up the austenite structure. Nevertheless, non-metallic inclusions can be seen beginning in the base material and continuing in the EA through the interface.

The surfaces' cross section has also been studied using the FIB technique. Through the erosion process originated in the sputtering of the surface using 5 keV Ga ions, cavities with controlled depths and with smooth polished lateral walls have been created.

By sample tilting (52° in our case) FIB observation of one of the lateral walls, i.e. the cross section of the surface layer, could be done.
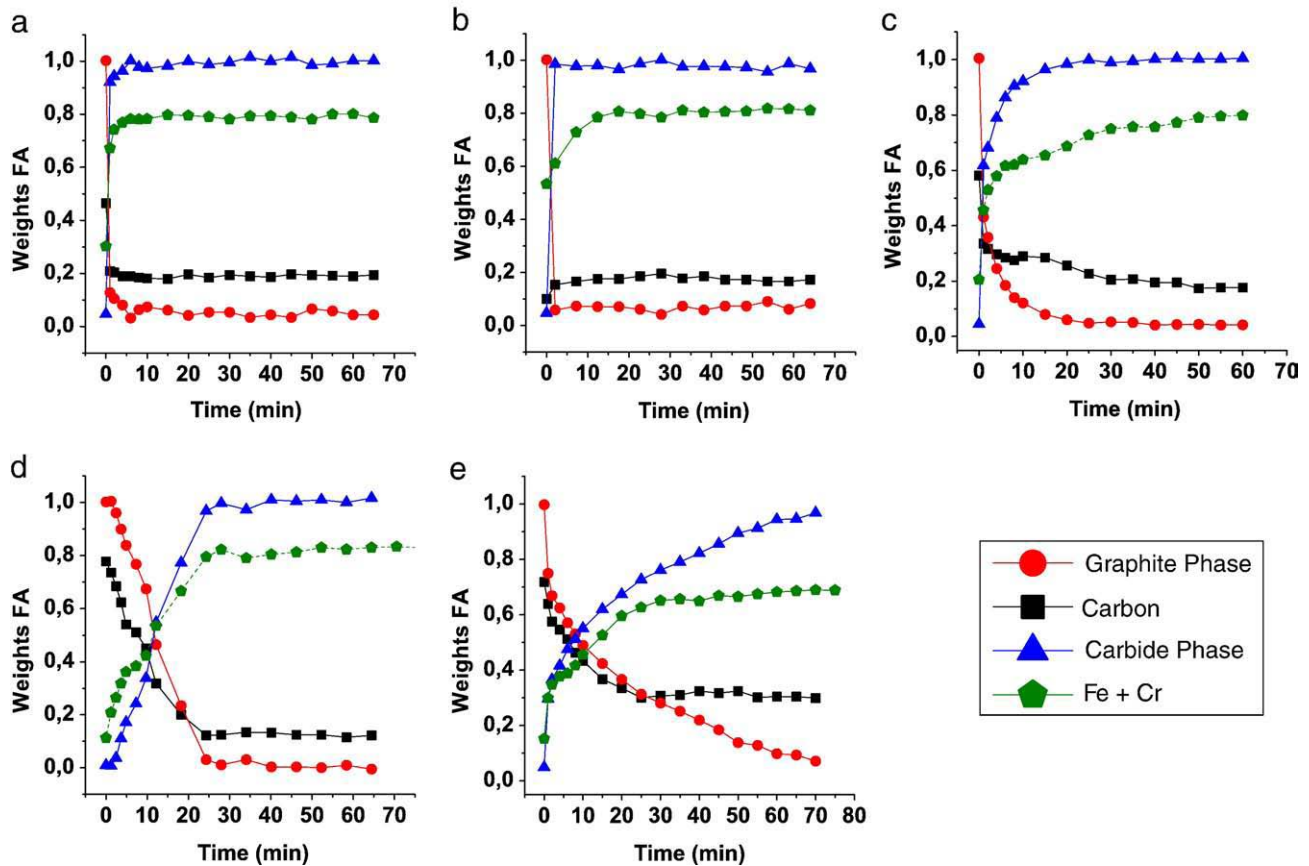
Fig. 5. Auger carbon concentration profiles for samples A1, A3, B1, B2 and B3 (parts a, b, c, d and e respectively). Black dots correspond to total carbon concentration. Triangles and circles correspond to carbon chemically bounded (as "carbide") and non-bounded (as "graphite") relative concentrations respectively. Fe + Cr concentration profiles are also plotted in each case to show the qualitative similitude with the ones for chemically bounded carbon.

On part a of Fig. 8 the FIB image of the cross section of the surface layer corresponding to a non-carburized AISI 316L ASS is displayed, showing the different crystallographic orientation of the grains through the different degree of gray (parallel bands 2–5 μm wide). This degree of gray is originated in the efficiency of secondary electron emission which will depend on the depth where the ion interacts with the atom of the crystal. Indeed, we can explain the image of the
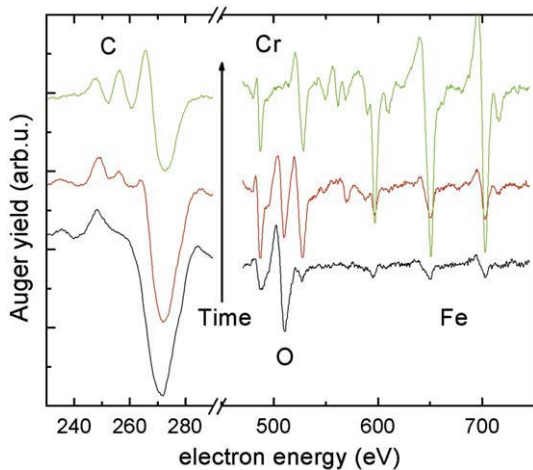

Fig. 6. Auger line shape evolution for 2 snapshots along B3 sample depth profile. Lower trace corresponds to the surface showing typical "graphitic" carbon. Upper trace corresponds to a typical "carbide" one. The trace in the middle corresponds to a mixture of both.

structures (part a of Fig. 8) as a consequence of the twin bands, with small re-crystallized regions, probably due to the effects of machining process during sample preparation, noticeable on the first half micron of the surface layer.

On the contrary, in the carburized sample A1 (part b of Fig. 8), a mosaic composed of structures with different levels of gray inside regular shaped regions can be observed. These structures can be attributed to defects, stacking faults and sliding band development due to the residual stresses induced during carbon diffusion into the material. These irregular patterns have typical sizes between 0.5 μm and 2 μm, meanwhile in the first half micron surface layer those domains turn out to be reduced to sizes between 0.1 μm and 0.5 μm. This is precisely the structure that cannot be seen through optical microscopy due to the resistance of the carburized steel to the electrochemical etching. Meanwhile in part a of Fig. 8 the image corresponds to a single grain, in part b instead, it is possible to see two different grains separated by a grain boundary nearly at the centre of the picture. On the other hand, no structures belonging to precipitates of carbides as reported in other papers (χ or Hägg carbides detected as needles perpendicular to the surface inside the austenitic matrix [13]) are observed in those images in agreement with XRD observations.

2.2.4. Hardness

Hardness surface's profiles were studied from the sample's top layer down to 1 mm depth. Closer to the surface, determinations were done through load versus penetration depth into the surface using nano-indentation tests (Berkovich test), with a load upper limit of 700 mN. Before testing, the surface's samples were ultrasonically cleaned in methanol and dried with infrared radiation for 3 min. For statistical purposes 10 tests were carried out on each type of sample. The results of
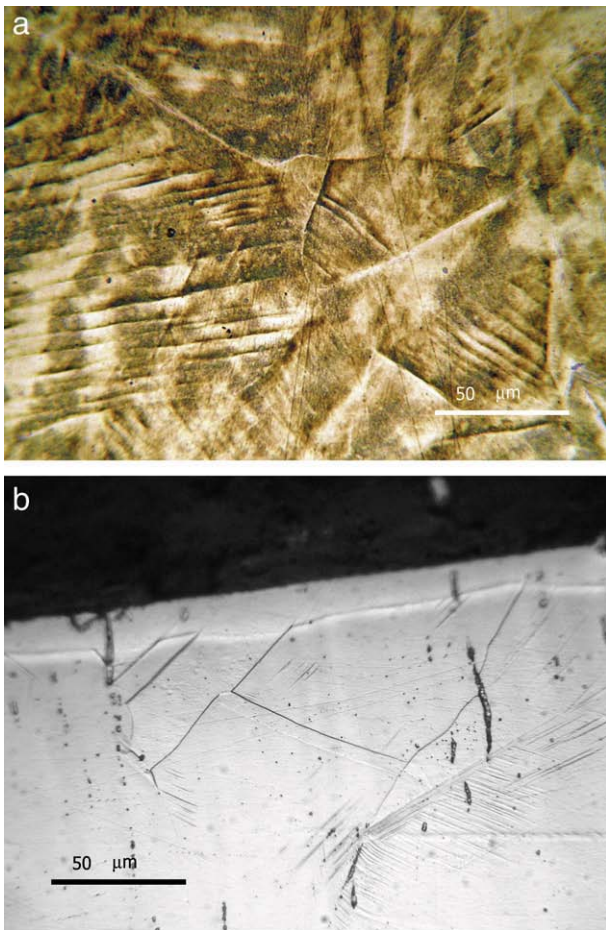
Fig. 7. Optical microscopy of sample A1. On part a, slip lines can be observed inside the individual grains. On part b, a cross section of the sample shows the EA surface layer over the austenitic structure of the bulk.
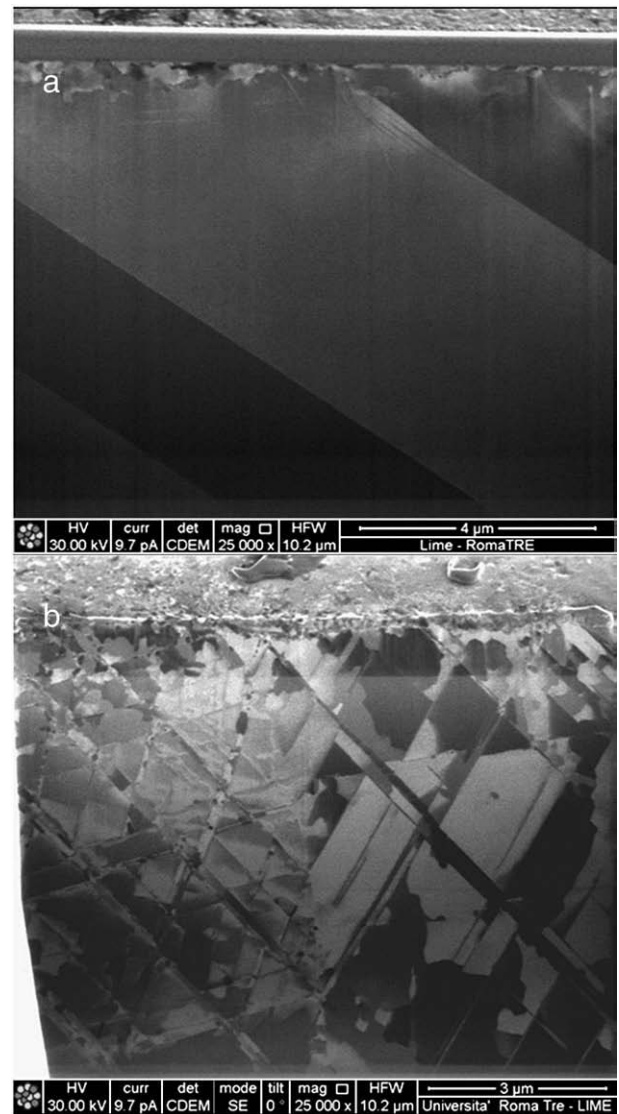

Fig. 8. FIB images of non-carburized AISI 316L ASS (part a) and carburized A1 (part b) sample's cross sections. Part a shows the existence of twins inside a grain of austenite, meanwhile in part b two grains showing an irregular structure inside each can be seen.

hardness H_{ns} are displayed in Fig. 9 showing a maximum H_{ns} of 11.8 GPa and 11.0 GPa for samples A1 and B1 respectively at ~200 nm depth, being reduced in both cases to ~8 GPa at ~2000 nm.

The nano-hardness profiles down to 140 μm were measured by nano-indentations (H_{nc}) on sample's cross section according to standard ISO 14577-1-2-3. For the tests, samples were cut and polished using the same technique described above. The results of H_{nc} are presented in part a of Fig. 10 showing the maximum of hardness of 7.5 GPa and 8.8 GPa for samples A1 and B1 respectively at a depth of ~15 μm. Beyond this 15 μm, and down to the studied depth (140 μm), the nano-hardness decreases down to ~5.4 GPa and ~5.2 GPa for samples A1 and B1 respectively.

To cover higher depth we have measured Vickers micro-hardness (HV) on the cross section using indentations with a load of 300 g. The hardness HV profiles are shown in part b of Fig. 10 in which every plotted value corresponds to an average of 12 measurements. Within the first 250 μm, the hardness was 2.9 GPa and 2.8 GPa for samples A1 and B1 respectively, reaching the substrate value of 2.55 GPa at ~1 mm depth.

2.2.5. Corrosion

Corrosion tests were done using ClNa 5.85% (weight in volume) solution. Samples of AISI 316L ASS were prepared and polished before ion carburization as described above for other tests. Carburized and non-carburized samples were immersed in a ClNa 5.85% (w/v) solution during 60 days at room temperature. After this period, samples were removed from the solution, rinsed with distilled water, ethanol and dried with hot air, and their surfaces inspected under optical microscopy and Scanning Electron Microscopy (SEM). The results on non-carburized samples did not show any damage associated to corrosion, with the surface remaining as removed from the polishing processes. Instead, for sample A1, the surfaces show gray spotty regions with few small pits consisting of ~80 μm diameter clouds composed of several ~5 μm diameter spots, as can be seen under optical microscopy on part a of Fig. 11. The rest of the surface is mainly composed of a less densely populated and almost uniformly distributed <0.5 μm size, with higher concentration along the grain boundaries and slip lines as can be seen through the SEM image on part b of Fig. 11. On the other hand, by observing the cross section image of part c of Fig. 11, it is possible to appreciate that the corrosion process is mainly superficial, not showing corrosion processes like channels going through the carburized layer. Nevertheless, for the case of sample B1, a generalized corrosion process (not shown in Fig. 10) has been observed.

2.2.6. Wear tests

To explore changes induced by carburization processes on tribological behavior we have used Ball-on-Disc wearing tests. Tests
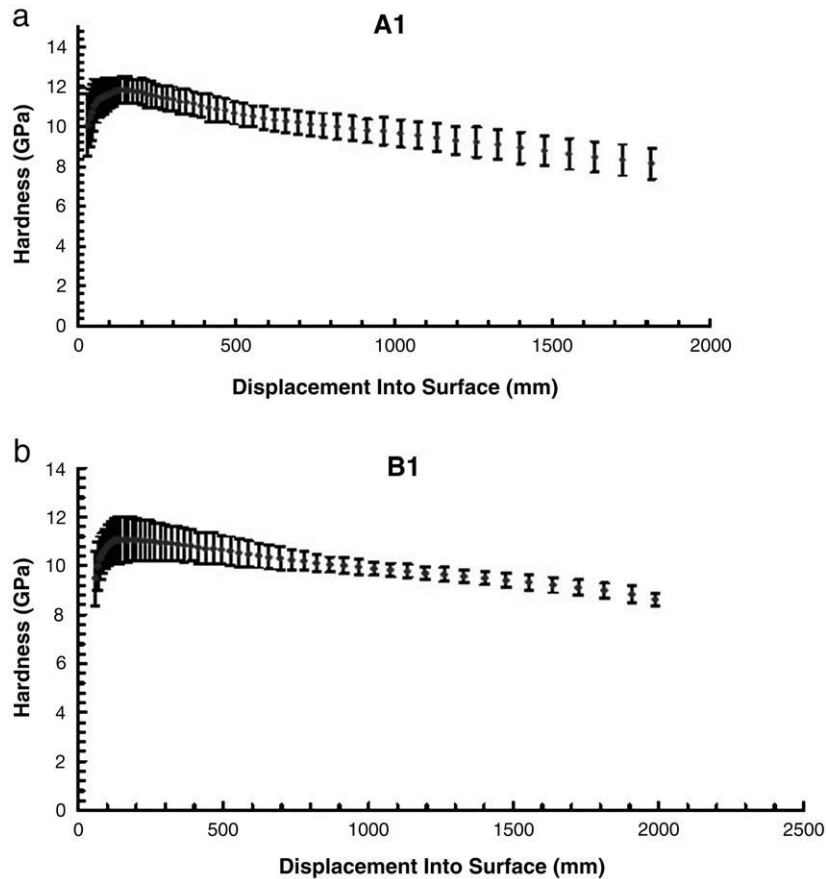
Fig. 9. Nano-hardness profiles determined through nano-indentations on top of the surface with different loads. Parts a and b correspond to samples A1 and B1 respectively.

were done with a Wazau TRM 100 tribometer in which the surface to be tested (disc shaped sample) rotates with constant angular velocity with period τ. At certain distance R of the centre of the sample, a fix ball of radius r is put in contact against the surface with a constant force F during rotation. After a time t, which will correspond to $N = t/\tau$ number of turns and a sliding distance $l = 2\pi R \cdot N$, the test is interrupted and the scar depth δ (*sagitta*) and the width of the track D (*chord*) left during the wearing process can be measured. With this information the exact volume for unit length S of the engraved scar can be calculated (using pure geometry calculations) considering that the scar profile can be approached to a section of a disc with radius equal to the radius r of the ball used in the tests. Then, S can be calculated as

$$S = \frac{1}{2} r^2 (\theta - \sin \theta),$$

where θ is the solid angle of a cone with the apex in the centre of the ball and base the resulting circle intersection between the surface of the ball and the surface of the sample, calculated at the end of the test. This circle has a diameter equal to D and θ will be equal to

$$\theta = \cos^{-1} \left(1 - \frac{D^2}{2r^2} \right).$$

In our work, we have used as a tribological pair a $r = 3$ mm alumina ball, with $F = 10$ N and τ selected in such a way that the relative velocity v of the ball against the surface along the track turns out to be the same for all tests, which in our case was $v = 0.1$ ms^{-1}. In Table 3 the parameters used for carburized samples A1, B1, B2 and B3 and for non-carburized material are indicated. The percentage $W_\%$ of

the volume removed on carburized samples regarding the non-carburized material can be calculated as:

$$W_\% = \left(\frac{S_i}{S_n} \right) \times 100,$$

where S_i and S_n are the volumes for unity length for carburized and non-carburized samples respectively. In Table 3 the values of S and $W_\%$ are also presented for comparative purposes.

The results have shown a reduction in the wear rate with ion carburization time for both gas mixtures used.

3. Discussion

We have shown that ion carburization of ASS in an Ar, H$_2$ and CH$_4$ gas mixtures has developed a hard and wear resistant surface layer. This surface improvement can be attributed to EA developed through carbon diffusion induced during the process. The EA was rapidly developed during the first 30 min of processing as can be seen in Table 2 and Fig. 2, period in which the lattice parameter has increased from 3.584 Å (corresponding to base material) to 3.660 and 3.654 Å for processing with Ar 50%, H$_2$ 45%, CH$_4$ 5%, and Ar 80%, H$_2$ 15%, CH$_4$ 5% gas mixtures respectively. For longer carburization times lattice parameters continuously increased but at lower rate, reaching the maximum lattice parameters 3.666 and 3.659 Å for both gas mixtures used. Those results, observed through GAXRD diffractometry, did not show any trace of carbides, which are in agreement with the results founded by Ernst et al. [18] when low-temperature (470 °C) gas-phase treatments of austenitic steels were practiced for time lapses ≤38 h. To sum up, although the total observed expansion has been ~5% higher for the richer in Ar gas mixture, for both gas mixtures
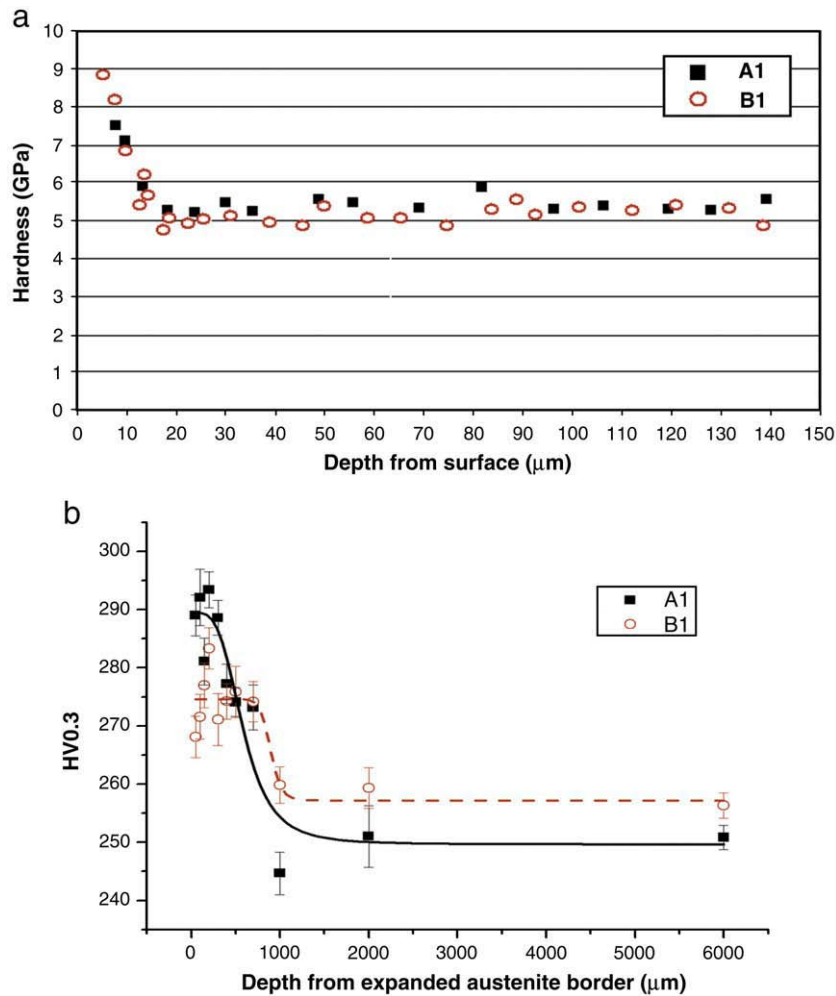
Fig. 10. a — Nano-hardness profiles of samples A1 and B1 determined using nano-indentations according standard ISO 14577-1-2-3. b — Vickers micro-hardness (300 g) profiles for samples A1 and B1.

lattice expansion with processing time has had a similar general behavior, consisting of an ~90% of the total observed expansion during the first 30 min.
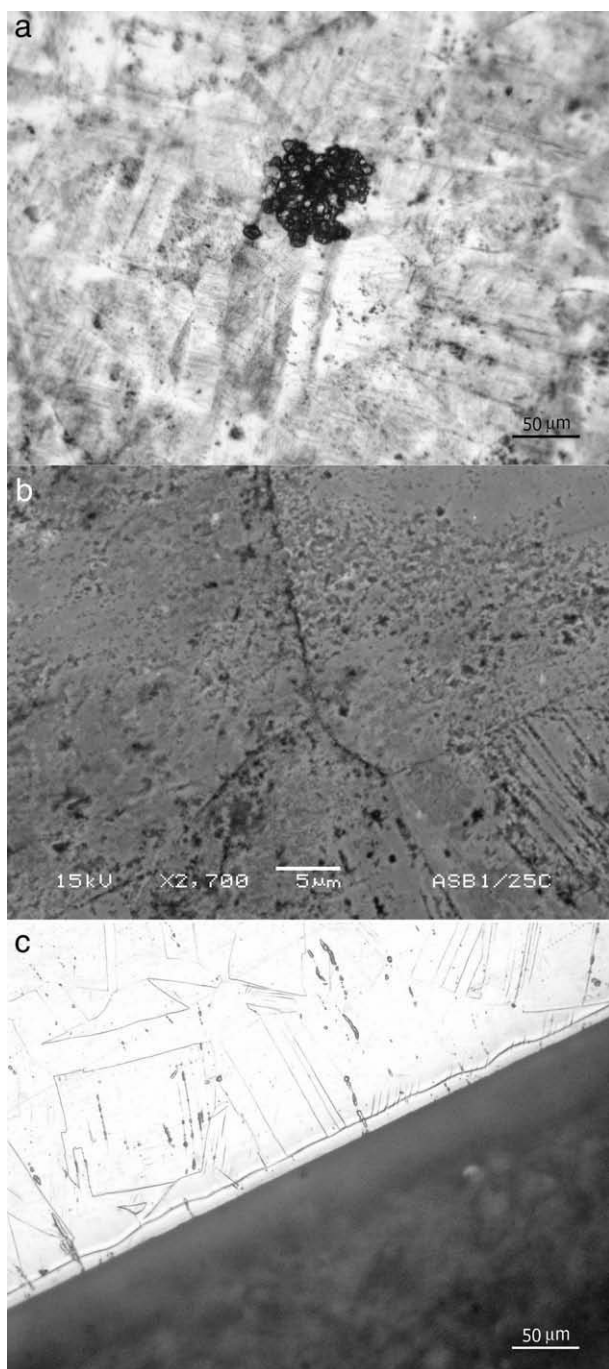
This rapid carburization behavior observed in our case was also observed by other authors using plasmas [5,9] and, as mentioned above, in a gaseous phase. This fact can be attributed to the processing temperature which is high enough to allow fast carbon inward diffusion but too low to induce mobility on Cr atoms, which are the ones with large chemical affinity with carbon atoms [13].

On the other hand, AES observations, which involve the first ~156 nm below the surface, have given different results to those corresponding to XRD that involves deeper layers. AES has shown the existence of chemically combined carbon. Indeed, during the first 30 min processing time, which corresponds the lapse in which EA had a rapid development, carbon becomes totally combined below the ~15 min sputtering on samples A1 and B1 as can be seen on parts a and c of Fig. 5, with free carbon only on top of the surface. For longer carburizing times no significant modifications have been found on the 50% of Ar reactive gas mixture used as can be seen on part b of the same figure, meanwhile important changes appear for the other gas mixture situation. Indeed, most of the extra carbon diffused is retained as free carbon (non-chemically bounded) with concentrations and depths that grow with processing time. Also, a difference in the chromium concentration profile evolution was found for both gas mixtures used. Meanwhile no substantial differences could be seen between samples A1 and A3, a chromium concentration increasing in

a surface layer down to a depth corresponding to ~22 min sputtering (with a maximum at the depth at 5 min of sputtering) was found. This chromium accumulation near the surface with processing time was already reported on ion nitriding of AISI 304L [26], and can be attributed to the selective sputtering of Fe and Cr due to Ar and carbon ions in our case (in place of nitrogen ions in case of Ref. [7]). Adding the concentration values of Cr and Fe for each situation (Figs. 3 and 4) we can see that the resulting profiles with depth (Fig. 5) have equivalent shapes to the carbon as carbide profiles. This fact agrees with the idea of carbon chemical binding to Fe and Cr on the surface layers studied with AES. The difference found with the two gas mixtures used, mixture in which the amount of the carbon source (i.e. methane) is the same, can be originated in the resulting current density during the processing, which is 8.1 mA cm^{-2} for samples B1, B2 and B3, and 7.0 mA cm^{-2} for samples A1 and A2. This current density can be traduced in the flux of carbon and Ar ions on the surface. Our results show that the strong effect on the carbon inclusion on the surface layers and the chromium accumulation with processing time were induced with ion fluxes resulting from density of currents higher than 7.0 mA cm^{-2}.

Going to deeper layers, the absence of carbide formation (carbon in solid solution, presumably in interstitial sites) observed in our case through XRD has also been determined in X5CrNi189 steel ion carburizing experiments using PIII operated in a methane gas atmosphere and at 400 °C [5]. Nevertheless other authors, using the same PIII technology but in AISI 304L ASS nitro-carburizing process

Fig. 11. Images of sample A1 showing corrosion patterns. a — SEM image of cloud of pitting; b — SEM image of pitting along grain boundaries; c — Optical microscopy of sample's cross section showing absence of corrosion penetration across interface.

Table 2

Processing time (min)	Gas mixture	
	50% Ar, 45% H$_2$	80% Ar, 15% H$_2$
0	3.584	3.584
30	3.660	3.654
60	3.661	3.669
120	3.666	3.659

passivating chromium oxide layer removal. They have found that with carburizing times between 26 and 38 h, carbon diffuses into the steel forming expanded austenite with a case 25 μm thick and a carbon concentration of 12%. Nevertheless, for longer carburizing periods higher carbon concentrations (above the 12%) can be obtained, with carbide precipitation as needles almost perpendicular to the surface observed in a heavily distorted austenitic matrix (EA). Further studies have shown that the precipitates are mostly constituted by Fe_5C_2 (χ phase or "Hägg" carbide), and their existence is within the first 7 μm below which the carbon remains in high concentrations (~10%) as in solid solution [25]. By observing our AES results, we can see that in addition to the fact that mostly of carbon is chemically bounded (carbide), its concentrations in all studied cases is above 12%, facts that are in agreement with the results of other authors [25,26].

The direct surface observation of carburized samples through optical microscopy has shown, for both carburization conditions, the existence of sliding bands, with morphology typical of a cold worked austenite, without grain deformation. On the other hand, by transversal observation, a typical surface layer of ~14 μm depth of EA could be seen, with an abrupt interface with the austenitic bulk of the steel. Some surface layer transversal observations had been done through FIB technique. For the non-carburized sample (part a of Fig. 7), parallels 2–5 μm wide bands can be seen showing the existence of twins inside the grain. On the other hand, FIB analyses of the carburized sample (part b of Fig. 7), in addition to this system of parallel bands, extra internal structures composed by defects, stacking faults and sliding bands could be seen. These defects can be attributed to the carbon inclusion in lattice inducing residual stresses, also responsible for hardness increases and tribological behavior improvements.

Indeed, the hardness is independent of the carburization conditions used, giving in both cases values up to ~11 GPa on top of the surface, and gradually decreasing down to the substrate values of ~2.55 GPa at ~1 mm depth.

As shown in Table 3, there was observed an improvement in wear behavior respect the base material in all cases. Nevertheless, and comparing results between carburized samples, it was found that wear rate was reduced following the sequence A1, B1, B2 and B3, which correspond to a gradual free carbon concentration and depth growing closer to the surface layers as observed in Fig. 5. We can assume that the amount of free carbon can play the role of solid lubricant, reducing the wear rate.

Considering that corrosion starts on grain boundaries and slip lines (as can be seen in the picture of part b of Fig. 10), it will result that the corrosion effect will be harder as the number of this high energy centres turn out to be higher. C. Blawert et al. [5] using PIII in an

with a mixture of N$_2$ and C$_2$H$_2$ at 350 °C, in addition to the γ_N phase have found Fe$_3$C formation [13]. In this sense, I. Lee [12] working on ion nitro-carburization of AISI 316L and AISI 304L stainless steels has found that the molybdenum into matrix made great contribution to depressing precipitations and promoting the diffusion of interstitial atoms like nitrogen and carbon during low-temperature plasma nitro-carburization. He found a limit temperature for CrN precipitation of 480 °C and 430 °C for AISI 316L and AISI 304L respectively, although no carbides have been found. A more detailed study of carbon diffusion into AISI 316L austenitic stainless steels have been done by F. Ernst et al. [13] using gas-phase carburizing at 475 °C with a previous

Table 3

Sample	R (m)	l (m)	N	D (m)	S (m^2)	$W_{\%}$
A1	9×10^{-3}	500	8842	0.93×10^{-3}	2.25×10^{-8}	60
B1	11×10^{-3}	610	8842	0.60×10^{-3}	0.60×10^{-8}	16
B2	5×10^{-3}	278	8842	0.59×10^{-3}	0.57×10^{-8}	15
B3	9×10^{-3}	500	8842	0.46×10^{-3}	0.27×10^{-8}	7
Non-Carburized	9×10^{-3}	500	8842	1.10×10^{-3}	3.74×10^{-8}	100

atmosphere of methane have found that ion carburized X5CrNi189 steel has developed a γ_C layer that had a behavior corrosion similar to the base material under acid (SO_4H_2) solution. In this carburizing condition, a carbon low super-saturation is produced with low defect densities induction. In spite of the differences between the carburizing method, the base material and the corrosive environment between our work (ClNa solution) and the one of reference [5], the higher degree of damage due to corrosion observed for sample B1 than for sample A1, can be explained through the argument given above. It is necessary to point out that in our case corrosion has become more important than the one observed by other authors [13]. The explanation can be funded in the fact that in spite we have developed EA down to a depth ~14 μm without carbide observations through XRD, the closer to the surface layers however have been shown carbide formation. X-ray penetrates deeper in the material than the observed layers through AES, resulting in the intensity of the diffracted X-rays corresponding to carbides that originated close to the surface layers, almost negligible. Carbide formation consumes the chromium of the surface resulting as a trigger to the chemical attack of NaCl solution as observed in our experiments.

4. Conclusions

EA development on AISI 316L ASS through ion carburizing at 405 °C with two different reactive gas mixtures (a — Ar 50%, H$_2$ 45%, CH$_4$ 5%, and b — Ar 80%, H$_2$ 15%, CH$_4$, 5%), and three different processing times (30, 60 and 120 min) have been studied. XRD results have shown fast (ion carburizing times <30 min) EA development down to ~14 μm depth. Optical microscopy observations have shown typical EA structure with sets of sliding bands on the surface. Transversal FIB observations have shown crystal reorientation domains inside the grains of austenite after carbon diffusion, but not carbide precipitation (needles) as observed by other authors [13]. Nevertheless, it has been found that for 30 min processing time in the layers closer to the surface (~150 nm) ~100% of diffused carbon is chemically bound for both gas mixtures used. In addition, while ion carburizing for periods >30 min has not shown significant changes for gas mixture a, gradual pure carbon concentration increase with processing time has been observed for gas mixture type b. Comparing our results with the ones reported using gas-phase low-temperature (475 °C) carburizing method, we could see that in spite the fact that in both cases there was EA development on the micrometer range surface layers, there is a significant difference on the layers closer to the surface (>150 nm). This difference can be attributed to the fact that in our case carbon and Ar ions arrive at the surface with kinetic energies and fluxes high enough to produce element concentration modifications through sputtering, a fact which is not present in gas-phase processing. Hardness profiles, from the first 100 nm near the surface to depths >1 mm, have shown similar behavior for both gas mixtures used, with hardness higher than the base material down to depths of ~700 μm, with the maximum of 12 GPa and 11 GPa at ~150 nm depth for samples carburized with gas mixture a and b respectively. Wear tests (Ball-on-Disc) instead have shown higher wear resistance for samples with higher processing times, such behavior can be attributed to the higher amount of free carbon found for higher processing times working as solid lubrication. Nevertheless, a particular situation arises with corrosion. Although EA had been proved to be resistant to corrosion, our results have shown a reduction with regard to the base material. The reason can be grounded in the existence of carbides on the surface, which are not corrosion resistant and can work as a trigger for corrosion. We can conclude that, while we develop EA 50 times more rapidly than through low-temperature gas-phase, with hardness increase and wear reduction, the ion flux present in our ion carbiding process has developed on the first hundreds of nanometer carbide source of worsening the corrosion behavior.

References

[1] A. Matthews, A. Leyland, B. Dorn, P.R. Stevenson, C. Bin-Sudin, M. Rebholz, A. Voerodin, J. Schneider, J. Vac. Sci. Technol. A 13 (1995) 1202.
[2] A. Leyland, K.S. Fancey, A. Matthews, Surf. Eng. 7 (1991) 207.
[3] P.A. Dearnley, T. Bell, F. Hombeck, in: T.S. Sudarshan, J.F. Barza (Eds.), Surface Modification Technologies VI, The Minerals, Metals & Materials Society, London, 1993, p. 143.
[4] J. Feugeas, B.J. Gómez, A. Craievich, Surf. Coat. Technol. 154 (2002) 167.
[5] C. Blawert, H. Kalvelage, B.L. Mordike, G.A. Collins, K.T. Short, Y. Jirásková, O. Schneeweiss, Surf. Coat. Technol. 136 (2001) 181.
[6] W. Möller, S. Parascandola, O. Kruse, R. Günzel, E. Richter, Surf. Coat. Technol. 116–119 (1999) 1.
[7] C. Blawert, B.L. Mordike, Y. Jirásková, O. Schneeweiss, Surf. Coat. Technol. 116–119 (1999) 189.
[8] J.R. Conrad, J.L. Radtke, R.A. Dodd, F.J. Worzala, C. Ngoc Tran, J. Appl. Phys. 62 (1987) 4581.
[9] D. Williamson, O. Ozturk, R. Wei, P. Wilbur, Surf. Coat. Technol. 65 (1994) 15.
[10] G. Abrasonis, J.P. Rivière, C. Templier, A. Declèmy, S. Muzard, L. Pranevicius, Surf. Coat. Technol. 196 (2005) 262.
[11] T. Czerwiec, H. He, G. Marcos, T. Thiriet, S. Weber, H. Michel, Plasma Process. Polym. 6 (2009) 401.
[12] I. Lee, Curr. Appl. Phys. 9 (2009) S257.
[13] F. Ernst, Y. Cao, G.M. Michal, A.H. Heuer, Acta Mater. 55 (2007) 1895.
[14] A.M. Abd El-Rahman, S.H. Mohamed, M.R. Ahmed, E. Richter, F. Prokert, Meth. Phys. Res. B 267 (2009) 1792.
[15] C. Blawert, B.L. Mordike, G.A. Collins, K.T. Short, Y. Jirásková, O. Schneeweiss, V. Perina, Surf. Coat. Technol. 128–129 (2000) 219.
[16] T. Czerwiec, H. He, S. Weber, C. Dong, H. Michel, Surf. Coat. Technol. 200 (2006) 5289.
[17] T. Christiansen, M.A.J. Somers, Scripta Mater. 50 (2004) 35.
[18] F. Ernst, Y. Cao, G.M. Michal, Acta Mater. 52 (2004) 1469.
[19] L. Nosei, M. Ávalos, B.J. Gómez, L. Náchez, J. Feugeas, Thin Solid Films 468 (2004) 134.
[20] L.E. Davis, N.C. MacDonald, P.W. Palmberg, G.E. Riach, R.E. Weber, Handbook of Auger electron spectroscopy, Perkin-Elmer, Eden Prairie, 1978.
[21] E. Malinowski, D. Howery, Factor analysis in chemistry, Wiley, New York, 1980.
[22] R.A. Vidal, J. Ferrón, Appl. Surf. Sci. 31 (1988) 263.
[23] L. Steren, R.A. Vidal, J. Ferrón, Appl. Surf. Sci. 29 (1987) 418.
[24] M.C.G. Passeggi Jr., L.I. Vergara, S.M. Mendoza, J. Ferrón, Surf. Sci. 507–510 (2002) 825.
[25] Y. Cao, F. Ernst, G.M. Michal, Acta Mater. 51 (2003) 4171.
[26] J.N. Feugeas, B.J. Gómez, G. Sanchez, J. Ferrón, A. Craievich, Thin Solid Films 424 (2003) 130.